Liquid-Liquid Interface Can Promote Micro-Scale Thermal Marangoni Convection in Liquid Binary Mixtures

Issei Aibara,[†] Tatsuki Katoh,[†] Chihiro Minamoto,[‡] Takayuki Uwada[§] and Shuichi Hashimoto*[,†,‖]

[†] Department of Optical Science, University of Tokushima, 2-1 Minami-Josanjima-Cho, Tokushima 770-8506, Japan.

[‡] Department of Applied Chemistry and Biotechnology, NIT Niihama College, 7-1 Yakumo-Cho, Niihama, Ehime 792-8580, Japan.

[§] Department of Chemistry, Josai University, 1-1 Keyakidai, Sakado, Saitama 350-0295, Japan.

[‖] Advanced Engineering Courses, NIT Gunma College, 580 Toriba-machi, Maebashi, Gunma 371-8530, Japan.

Abstract

Liquid-liquid phase separation, a physical transition in which a homogeneous solution spontaneously demixes into two coexisting liquid phases, has been a key topic in the thermodynamics of two-component systems and may find applications in separation, drug delivery, and protein crystallization. Here we applied a microscale temperature gradient using optothermal heating of a gold nanoparticle to overcome the experimental difficulties inherent in homogeneous heating: we aimed at highlighting precise structural development by avoiding randomly nucleating/growing microdomains. In response to laser illumination, a single gold nanoparticle immersed in a binary mixture of aqueous 2,6-dimethylpiridine (lutidine) and *N*-isopropylpropionamide (NiPPA) was clearly sensitive to the phase transition of the surrounding liquid as demonstrated by light scattering signals, spectral red-shifts and bright-spot images. The local phase separation encapsulating the gold nanoparticle resulted in immediate formation and growth of an organic-rich droplet which was confirmed by Raman spectroscopy. Remarkably, the droplet was stable under a non-equilibrium steady-state heating condition because of strong thermal confinement. Microdroplet growth was ascribed to thermocapillary flow induced by a newly formed liquid-liquid interface around the hot gold nanoparticle. Based upon a tracer experiment and numerical simulation, it is deduced that the transport of solute to the high temperature area is driven by this thermocapillary flow. This study enhances our understanding of phase separation in binary mixtures induced by microscale temperature confinement.

1
2
3
4
5
6
7
8
9
10
11
12
13
14
15
16
17
18
19
20
21
22
23
24
25
26
27
28
29
30
31
32
33
34
35
36
37
38
39
40
41
42
43
44
45
46
47
48
49
50
51
52
53
54
55
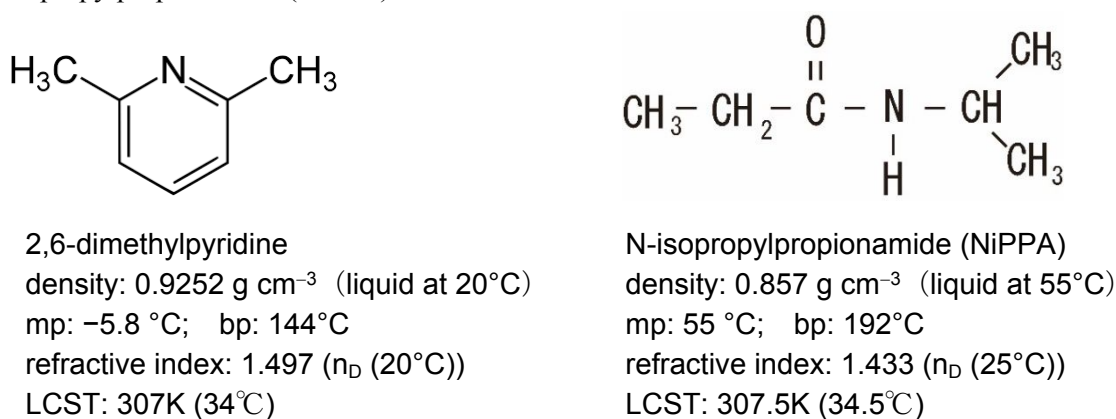56
57
58
59
60

Introduction

Liquid-liquid phase separation, in which a homogeneous solution spontaneously demixes into two coexisting liquid phases, has been key to understanding the thermodynamics of two-component systems.[1-3] It is also important in applications such as protein crystallization, which is postulated to proceed via a two-step process involving the formation of liquid droplets of high protein concentration to generate ordered protein clusters within the dense liquid intermediate prior to nucleation, leading to protein crystals.[4,5] Moreover, droplets formed as a result of the liquid-liquid phase separation of proteins play important roles in cell biology, such as the processes of transcription and translation, control of signal transduction, responses to environmental stress, and amyloid formation, to name only a few.[6-8]

Experimental studies of temperature-induced phase separation in binary liquids have been limited to bulk solutions heated in large volumes despite the fact that the phenomenon starts at the molecular nano-scale level, before propagating to the entire solution. To elucidate the early stage of phase separation, transient temperature-jump spectroscopy has been applied under the optical microscope with structured illumination, seeking resolution below the limits of diffraction.[9] Although the instrumentation is still under development, such experimental observation was able to reveal the phase separation dynamics from micellar-like aggregates to a periodic structure for a 2-butoxyethanol/water binary mixture.[9] Besides the transient temperature jump in the bulk of the solution, application of a temperature gradient is expected to provide a means to clarify the dynamics of phase-separating molecules at small scales. Such an investigation has been performed for the coarsening of solvent structure around a colloidal particle emerging after temperature quenching of the colloidal surface using a mesoscopic numerical simulation.[10] It was predicted that, upon phase separation, concentric multi-ring structures of binary mixtures develop with time. To observe experimentally the effect of a local temperature gradient on liquid-liquid phase separation, optical

3

heating of a single gold nanoparticle (Au NP) is appropriate because such a technique can induce

highly localized heating at scales from the diffraction limit to microscale. Continuous laser heating

of an individual Au NP results in a well-defined steady-state temperature profile, $\Delta T \propto r^{-1}$,[11] which

may induce phase separation in the environment around the particle.

In the experiments reported here, the liquids chosen to demonstrate phase separation were

aqueous 2,6-dimethylpyridine (2,6-lutidine, abbrev.: lutidine) and *N*-isopropylpropionamide

(abbrev.: NiPPA). The relevant chemical structures and physical constants are provided in **Scheme**

1.

Scheme 1. Chemical structures and relevant physical constants of 2,6-dimethylpyridine (lutidine) and *N*-isopropylpropionamide (NiPPA).

2,6-dimethylpyridine
density: 0.9252 g cm^{-3} (liquid at 20°C)
mp: −5.8 °C;   bp: 144°C
refractive index: 1.497 (n_D (20°C))
LCST: 307K (34℃)

N-isopropylpropionamide (NiPPA)
density: 0.857 g cm^{-3} (liquid at 55°C)
mp: 55 °C;   bp: 192°C
refractive index: 1.433 (n_D (25°C))
LCST: 307.5K (34.5℃)

Previously, homogeneous heating-induced liquid-liquid phase separation has been investigated for a

lutidine/water mixture, and the phase diagram obtained.[12-14] At temperatures below the critical

temperature, referred to as the lower critical solution temperature (LCST: 34°C; 307 K), lutidine

solution is completely miscible, forming a clear single phase. At temperatures above the LCST, the

solution turns turbid due to nucleation occurring at binodal and spinodal transitions, depending on

the composition and rate of variation in temperature, $\Delta T/\Delta t$. Spinodal decomposition produces

bicontinuous wormlike structures, eventually followed by demixing to two phases. For aqueous

NiPPA, temperature-induced phase separation has been demonstrated to occur at an LCST

4

of 34.5°C (307.5 K).[15,16] The LCST properties of this category of binary solutions (aqueous amines) are ascribed to hydrogen-bonding between water and the organic amines: strong hydrogen bonds promote mixing below the LCST, whereas above the LCST such hydrogen bonds undergo rupture because of thermal fluctuation at high temperatures.[17]

We use the photothermal effect of a single Au NP to trigger and maintain the state of nonequilibrium phase separation for binary liquids. Upon photoexcitation of their localized surface plasmon resonance (LSPR) bands, Au NPs absorb incident light and turn into efficient nano-heat sources which can be managed remotely by manipulating the light. This fundamental scheme of photothermal effect has found numerous applications in physics, chemistry and biology at micro and nano scales.[18-21] In this study, using a protocol of photothermal temperature confinement, we aimed at creating a strong temperature gradient in the local environment of a Au NP, allowing the temperature to increase above the LCST only in a limited volume. Application of a local temperature jump instead of spatially homogeneous heating can generate a temperature field strongly coupled to the local composition of a binary mixture and may alter the mechanism of phase separation.

Methods

Experimental. We used dark-field imaging on an inverted microscope with a dark-field condenser equipped with a CMOS camera (**Scheme 2**). A halogen lamp with a broad (white) spectrum was used as a source of illumination for recording the scattering images. Single Au NPs (see Supporting Information S1 for a particle image and histogram) adsorbed on the lower surface of an upper substrate (ceiling) or the upper surface of a lower substrate (floor) and submerged in solutions of lutidine and NiPPA in a closed chamber (11 µL) were heated by illuminating a focused 488-nm CW laser beam through the microscope objective lens (see Supporting Information, S2 for the physical properties of lutidine/water and NiPPA/water). Single-particle scattering spectra were recorded on a dark-field microscopy-spectroscopy setup at a wavelength resolution of 0.5 nm (**Scheme 2**). Raman spectroscopy under laser-heating of a Au NP was also performed with an

5

excitation wavelength of 637 nm. For further details, including the method of sample preparation, see Supporting Information S3.

Numerical simulation. A commercial finite-element mode solver, COMSOL Multiphysics Ver. 5.4b (http://www.comsol.com), was used for temperature estimation and convective flow analysis under illumination with a laser beam focused on single Au NPs. Details of the procedure are provided in Supporting Information S4.

Scheme 2. Setup for optical measurements. For laser illumination, two Au NP configurations were used, ceiling (left) or floor (right).
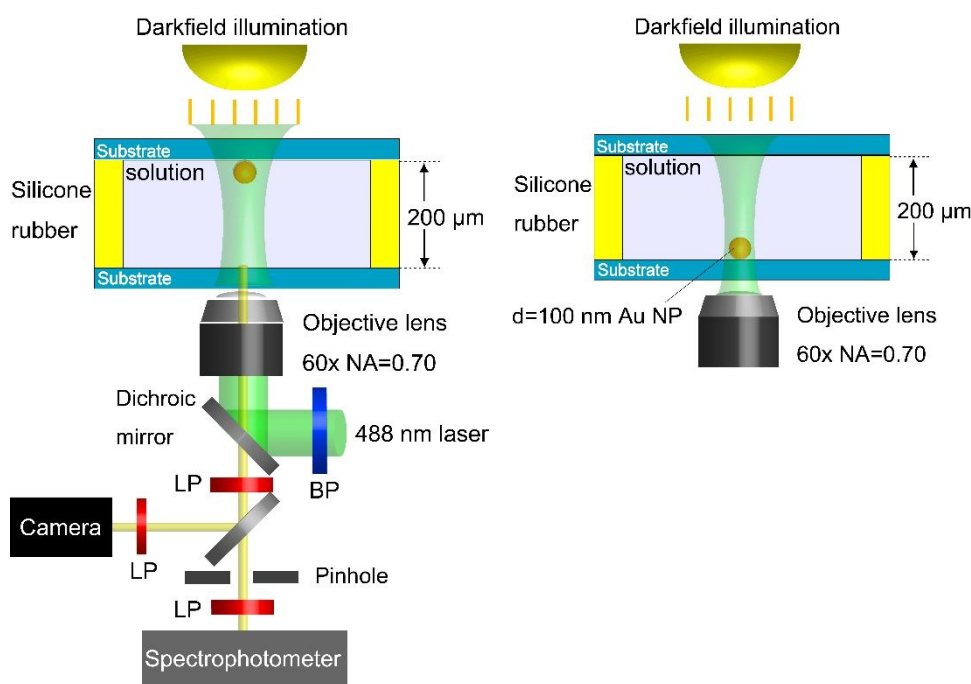
Results and Discussion

A. Observation of a liquid droplet from light-scattering spectral measurements and dark-field imaging.

Dark-field microscopy and spectroscopy were used to investigate the demixing behavior of binary mixtures. The demixing transition should cause refractive-index changes that can be monitored by dark-field images at the micrometer scale. Moreover, such medium refractive-index changes induce shifts in the light-scattering spectra of Au NPs because the plasmonic Au NPs support the LSPR which is sensitive to the medium refractive index.[22] Thus the spectral measurement can provide information relevant to the nanoscale structural changes of binary mixtures initiated by temperature-induced phase transition in the immediate neighborhood of a Au NP. As a control experiment, we measured the single particle light-scattering spectra of a Au NP as a function of lutidine %w/w in water. The scattering peak wavelength *vs*. lutidine %w/w is depicted in Supporting Information, Figure S5. Progressive spectral red-shifts, dependent on the increasing refractive index of the surrounding medium, were observed. Scattering spectral simulation based on Mie calculation suggested that the red-shifts are consistent with the medium-dependent optical properties of a Au NP.[22]

   Figure 1 shows the laser intensity-dependent dark-field images and light-scattering spectra of a 100-nm-diameter Au NP exposed to a 20-%w/w (4.0 mol%) lutidine/water mixture upon laser excitation at a wavelength of 488 nm. The laser illumination was focused on a single Au NP of interest. The measurements were performed before, during, and after laser illumination. Figure 1a shows a series of light-scattering images of a Au NP. Before laser illumination, the image of the Au NP was a diffraction-limited spot of ~0.7 μm (far left). When the laser is on, the bright light-scattering spot clearly expanded from that of the original Au NP, showing an emerging high refractive index body surrounding the NP. When the laser is off (Figure 1a, far right), the Au NP image is quite similar to
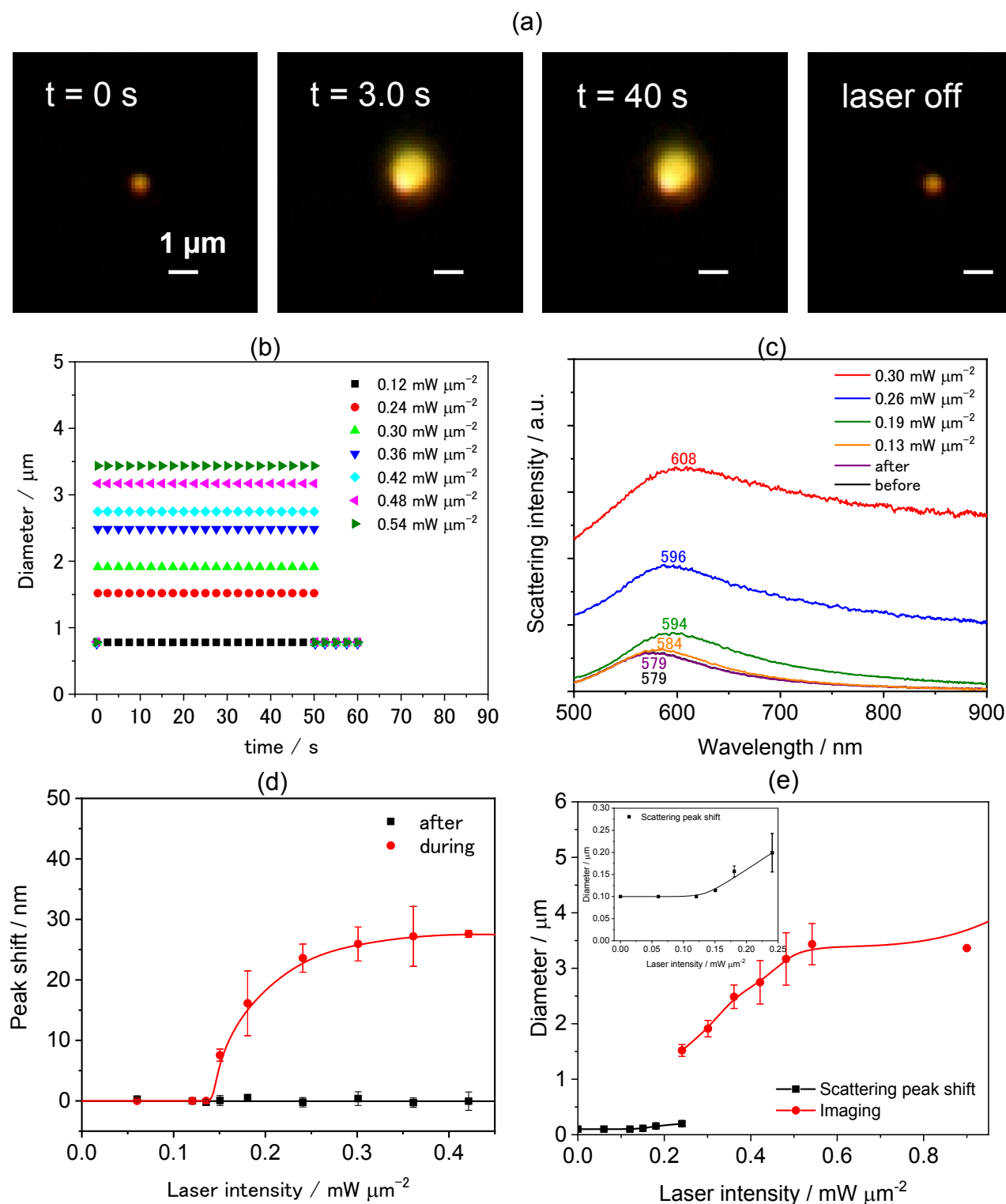
7

Figure 1. (a-c) Dark-field imaging and spectroscopy of a 100-nm-diameter Au NP exposed to 20 %w/w (4.0 mol%) lutidine/water mixture on focused laser excitation at 488 nm. (a) Light-scattering images before, during, and after laser illumination at 0.24 mW μm^{-2}. (b) Diameter vs. exposure time of the light-scattering spot at various laser intensities. Errors: within ±10%. Laser intensity-dependent light-scattering spectral changes (c), and spectral peak shifts (d). (e) Diameter vs. laser intensity curve obtained from both scattering spectral shift and imaging. In (d) and (e), solid lines are drawn by eye as a visual guide. Note that 1.0 mW μm^{-2} = 10^5 W cm^{-2} = 10^9 W m^{-2}.

8

that obtained before illumination. Figure 1b shows the diameter of the light-scattering spot obtained

from the dark-field images as a function of laser-illumination period at various intensities. On starting

illumination, the diameter increased instantaneously (within the response time of the camera of 0.25

s) and then remained constant. Further, the diameter of the scattering spot increased as a function of

laser intensity. On terminating laser illumination, the light-scattering spot returned to the original Au

NP size, suggesting that it underwent no permanent size increase.

Figure 1c shows the light-scattering spectra at various laser intensities. Before irradiation, the

spectrum is typical of LSPR scattering from a single Au NP.[22] The refractive index of a 20-%w/w

solution is 1.372, which is slightly larger than that of water, 1.332 (Supporting Information, Figure

S2-1c). As laser intensity was increased, there were gradual increases in both spectral red shift and

background scattering intensity; the former originating from a Au NP surrounded by a medium with

an increasing refractive index; the latter is ascribed to the gradually increasing size of light-scattering

medium adjacent to the Au NP (Figure 1a). Figure 1d shows the spectral peak shift (red shift) as a

function of laser intensity based on Figure 1c. Importantly, the spectral shifts observed are completely

reversible: the spectral shifts and intensifications occurred only during laser illumination. Starting at

0.15 mW μm^{-2}, the spectral red-shift increased with increasing laser intensity and saturated at 0.4 ~

0.5 mW μm^{-2}.

The observed scattering spectral changes, both the LSPR red-shift and increased base, can be

interpreted by the encapsulation of a Au NP in a lutidine-rich droplet, the thickness of which increases

depending on the laser intensity and lutidine concentration. To assess the effect of encapsulation on

the scattering spectral changes, we performed a spectral simulation applying the Mie formalism for

spherical particles[23] (Supporting Information Figure S6). In the Mie calculation, a concentric

spherical Au NP core–lutidine-rich shell structure dispersed in water was assumed with various shell

9

thicknesses (see Figure S6a). We assumed the refractive index of the lutidine shell to be 1.45, that is, slightly smaller than 1.497 of neat lutidine because the phase-separated lutidine droplet may contain some water, the amount of which is not accessible. The amount of red shift was found to saturate at greater shell thicknesses, so the droplet diameter estimation is limited to a shell thickness of < 100 nm. It should be noted that the contribution of substrate to spectral changes is not included here. A numerical simulation based on the finite element method (FEM), which includes the contribution of a substrate, can be performed using COMSOL MultiPhysics. However, we found that the FEM computation requires considerable computational time, far from practical use. For estimation of approximate shell thickness, the Mie calculation should suffice.

To reveal the chemical composition of a droplet, we performed a Raman spectroscopic study of the light-scattering spot under Au NP heating (Supporting Information, S7). First, we measured the spectra of lutidine/water mixtures at various concentrations of lutidine (Figure S7a). The Raman intensity ratio of $I_{2900\text{cm}^{-1}}$(lutidine)/$I_{3400\text{cm}^{-1}}$(H_2O) increased with increasing contribution of lutidine, so this ratio can be a good measure of lutidine concentration. With this in mind, we looked at the spectral change occurring when a laser is used to illuminate a Au NP in 20 %w/w lutidine in water (Figure S7b). Upon illumination with the heating laser (488 nm) colinearly with the Raman probe laser (637 nm), the intensity ratio of lutidine to water increased markedly. The concentration of lutidine in a droplet estimated from the control experiment was 30-40%. This result clearly supports the notion that the light-scattering spot formed on laser illumination is a lutidine-rich droplet resulting from phase separation. However, the lutidine concentration estimated is much lower than that expected from the phase diagram (Figure S2-1a). This may arise from the interference of Raman signal from bulk solution because of the small size of the droplet formed. Although qualitative, the Raman spectroscopic study confirmed the occurrence of phase separation giving rise to a lutidine-rich droplet.

The droplet diameters obtained from spectral red-shifts were plotted as a function of laser intensity and diameters determined from imaging (Figure 1e, black and red dots, respectively). The

10

droplet diameters obtained from the spectral shifts are useful for nano sizes at low laser intensities, and those obtained from imaging can be used for droplets over diffraction-limited sizes. Strictly speaking, the droplet diameters obtained from the two methods at 0.25-0.3 mW μm^{-2} did not correspond, which is a limitation of both methods: the imaging method is not good at estimating diameters near diffraction-limited sizes; and the spectral-shift method is poor at estimating droplet diameters > 200 nm. Overall, the droplet diameter increased with a threshold at 0.15 mW μm^{-2} and saturated at laser intensities > 0.6 mW μm^{-2}.

Figure 2 shows the laser-intensity-dependent light-scattering spectral changes of a 100-nm-diameter Au NP exposed to 50-%w/w (14 mol%) aqueous NiPPA, which has a refractive index of 1.42 before irradiation (Supporting Information, Figure S2-2c). Because of the relatively high refractive index of the medium, the light-scattering spectrum of the unirradiated solution was red-shifted compared to the 20-%w/w lutidine/water mixture in Figure 1. Upon irradiation, the scattering spectrum underwent initially red shifts suggesting an increased refractive index of the surrounding medium. Besides the shifts, the spectral intensity increased as for the lutidine/water mixture because of the increased size of the high-index medium formed around the Au NP, but only small red-shifts were observed. Given that the spectral red-shifts are not as marked as those in the lutidine/water mixture because the refractive index is already greater than that of the lutidine/water mixture, we used laser intensities up to 1.0 mW μm^{-2}. However, the light-scattering spectra underwent blue-shifts instead of red-shifts at higher intensities. We also observed a spectral blue-shift in pure water, which increased with increasing laser intensity. This was caused by temperature-induced refractive-index reduction of the medium.[24] The temperature-induced blue-shift was found to be greater in 50-%w/w aqueous NiPPA than in pure water. Because of this temperature effect, we could only observe small
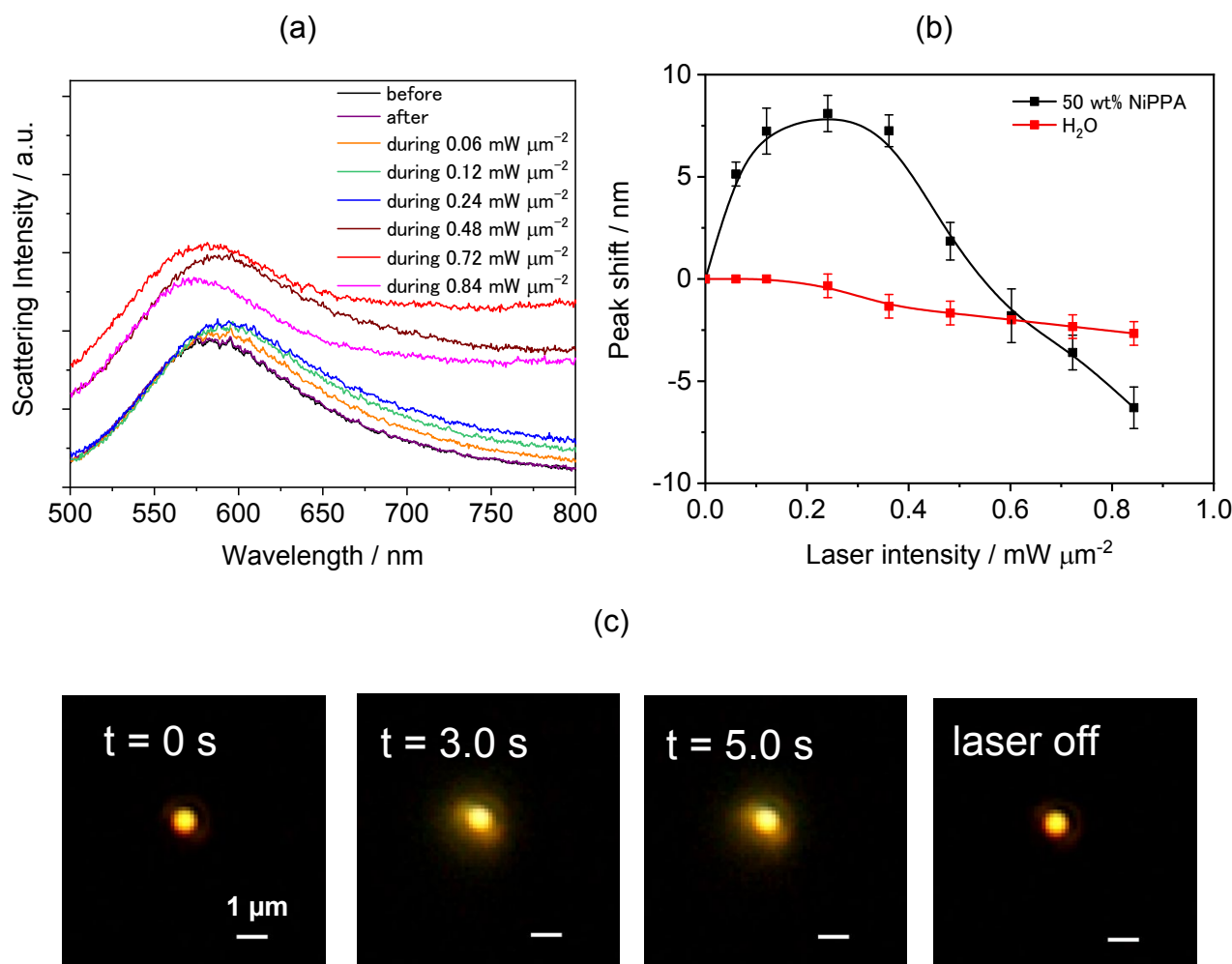
11

(a)

(b)

(c)

Figure 2. (a, b) Light scattering spectroscopy of a single Au NP in 50-%w/w (14 mol%) NiPPA/water mixture upon focused laser illumination at 488 nm: laser intensity-dependent light-scattering spectral changes (a), and spectral peak shifts (b). In (b), light scattering spectral peak shifts of a 100-nm Au NP in pure water is included for comparison and solid lines are drawn as a visual guide. (c) Dark-field imaging of a 100-nm-diameter Au NP in 50 %w/w (14 mol%) NiPPA/water mixture upon focused illumination with a laser intensity of 0.36 mW μm^{-2} at 488 nm.

----

red-shifts for NiPPA at limited laser intensities (0.05–0.5 mW μm^{-2}). However, the basic conclusion is not altered for Au NP heating in NiPPA/water, which is similar to that in a lutidine/water mixture: phase separation occurred forming a NiPPA-rich droplet encapsulating a Au NP. For a 50-%w/w aqueous NiPPA that undergoes phase separation passing through LCST, the refractive index contrast was insufficient for imaging. The series of dark-field images shown in Figure 2c depict the droplet

12

formation. In this case, a double ring structure was observed, with a much brighter inner ring and less bright outer ring. The origin of this double ring structure can be ascribed to the temperature profile around a Au NP: higher temperatures nearer the particle than the outer region may facilitate the dehydration of NiPPA molecules. We tried to control the thickness of the ring structure by modifying the laser intensity but failed. More sophisticated control will be required in future studies. Previously, a concentric ring pattern consisting of alternating low and high concentrations was proposed to occur based on a simulation study.[10] However, such a periodic structure was not observed in our study, presumably because of interference by convective flow (see section B).

B. Observation of liquid flow upon heating a supported Au NP

Here we investigate a potential liquid flow that can be relevant to the observed phase separation when a Au NP supported on a wall is laser-heated inside a sample chamber. For this purpose, 600-nm-diameter polystyrene (PS) particles were suspended as a tracer in lutidine/water mixture and water. Without illumination, slow random motions of the PS particles were observed because of thermal Brownian motion. When the laser illuminated a supported Au NP in 20-%w/w lutidine/water in the ceiling configuration, PS particles floating close to the Au NP were attracted and accelerated toward it (Supporting Information, S8). The observed migration velocities were measured by analyzing sequential images. The migration velocities of PS particles were found to depend on both the laser intensity and the radial distance from the heating center, Au NP. **Figure 3** shows the velocities dispersed in lutidine/water, in comparison with those dispersed in water as a function of radial distance from a Au NP. Figure 3a shows that the migration velocities are nearly constant at sufficiently large distances, but a sudden acceleration was observed at distances below 10 μm at a laser intensity of 0.90 mW μm^{-2}. At a higher intensity (1.2 mW μm^{-2}), an increased velocity occurred at around 20 μm. However, in water (Figure 3b), there was no apparent difference in migration velocity with distance from a hot Au NP at a laser intensity of 1.2 mW μm^{-2}. Note that PS particles in water were found to be strongly pulled to a Au NP when very close to it (approximately the size

13

of the laser beam diameter). However, it was difficult to estimate the migration velocity of PS

particles close to the Au NP, so points with accelerated velocities could not be added to Figure 3b.

The striking contrast in motion in response to Au NP heating between PS particles in lutidine/water

and those in water originates from the liquid-liquid interface formed in binary mixtures, as will be

explained in section C. Obviously, we can assume that the transport of PS particles is caused by

phoretic motion with the liquid flow rather than a self-propelled motion. As PS particles are known

to be thermophobic, they tend to move down a temperature gradient, away from the hot area.[25,26] They
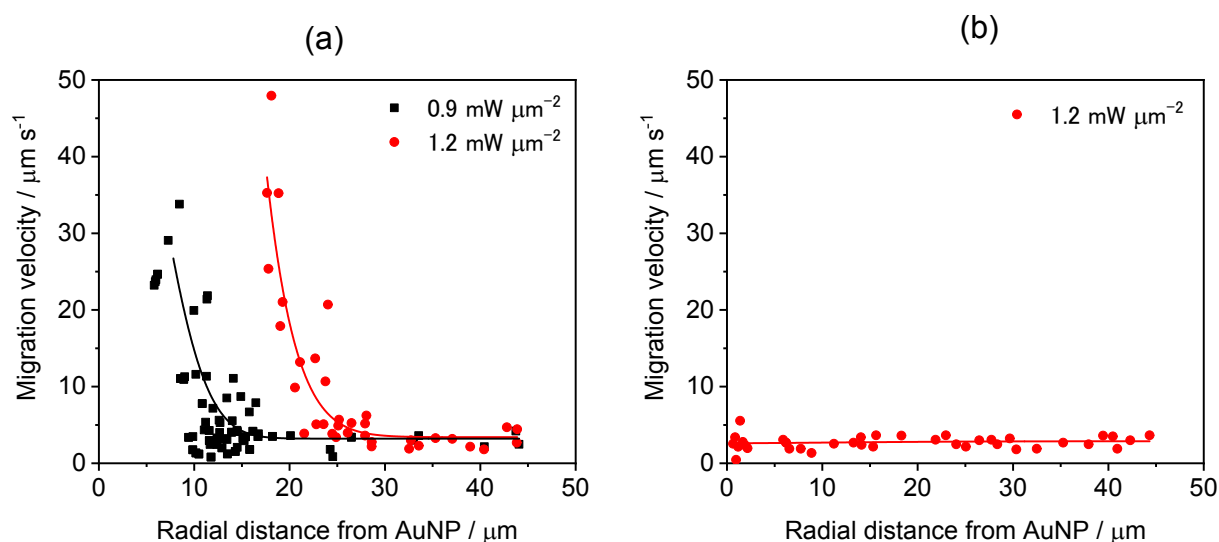
can move to the hot Au NP only while riding a liquid flow.

Figure 3. Migration velocity of PS particles (diameter: 600 nm, concentration: 9×10^7 particles mL^{-1}) as a function of distance from a heat source (100-nm-diameter Au NP) for a liquid film thickness of 200 μm in 20 %w/w lutidine/water mixture (a), and in water (b). Au NPs were supported on the substrate in the ceiling configuration. Solid lines are drawn by eye as a visual guide. Errors in measured velocities: within ±10%.

Previously, silica particles of 500 nm diameter have been observed to move in the direction of

a Au NP that was laser-heated in a closed chamber filled with water.[27] In that experiment, a nano- or

micro-sized bubble was formed around the Au NP, and the driving force of microparticle migration

was ascribed to Marangoni convection along the air-water interface from the hot substrate surface to

the cold bubble apex. As the silica particles approached the Au NP moving along the substrate surface,

both the Au NP and silica particles were imaged in focus. However, PS particles in lutidine/water

14

move differently. In the ceiling configuration, the PS particles staying vertically away from the substrate surface approached and were sucked in toward the Au NP. Thus, when we focused the objective on the Au NP, the image of PS spheres migrating toward it were out of focus (see Supporting Information, Figure S8). This may mean that PS particles approached the Au NP a few micrometers below the Au NP, not along the substrate surface. This is discussed further in section C based on flow simulation.

C. Mechanistic Insight into the Au NP heating-induced phase separation

The observed LSPR red-shifts and a bright light-scattering spot surrounding a Au NP, as well as the Raman spectral change, strongly suggest that a phase-separated organic droplet is formed encapsulating the Au NP when heated photothermally in binary solutions. Previously, homogeneous heating-induced phase separation has been shown to occur ubiquitously in lutidine/water and aqueous NiPPA, resulting initially in a milky white solution and eventually two separated phases: organic-rich and water-rich phases.[12-17] In our experiment, phase separation occurred site-specifically only adjacent to the hot Au NP, forming an organic-rich microdroplet with a high refractive index. It is reasonable to assume that the phase separation sets in at laser intensities just above the threshold that brings the temperature of medium immediately neighboring the Au NP to the LCST of 307 K. For example, for 20-%w/w lutidine/water, the threshold laser intensity was 0.15 mW μm^{-2} (Figure 1b). We estimated the particle temperature under continuous laser illumination as a function of laser intensity (Supporting Information S9) using a numerical simulation because an experimental temperature determination has yet to be established.[28,29] The temperature increase was expected to occur dependent on laser intensity both for a Au NP and the surrounding medium. The calculated threshold temperature at which the scattering spectral red-shift occurred (0.15 mW μm^{-2}) was 308 K, a value which agrees reasonably well with the known threshold temperature of phase separation, 307 K. On illumination, we observed that the phase-separated microdroplet grew in size with time: the growth rate was fast, within 1−2 s, close to the time resolution of our camera. The diameter of the

15

microdroplet increased with an increase in laser intensity (Figure 1b). Here we attempt to explain step by step the process of phase-separated droplet formation.

Firstly, the initial process of droplet formation is triggered by laser heating of a Au NP. At the very beginning, small-scale phase-transition can occur in solution in contact with the surface of a hot Au NP. When the liquid temperature surpasses the LCST, organic aggregates will form resulting from the rupture of hydrogen bonds between the organic amines and water molecules,[17] followed by association through hydrophobic interaction. These aggregates only form in close to the hot Au NP and remain because of temperature confinement around the Au NP. This temperature confinement originates from the temperature distribution around a hot Au NP, which decreases with distance from the particle center following a radial temperature profile, $\Delta T \propto r^{-1}$, before declining to ambient temperature.[11] The temperature confinement is also responsible for further aggregation to form a thin layer of lutidine-rich or NiPPA-rich phase surrounding the Au NP because of greater instability of the amine-rich phase as the medium temperature is higher. Additionally, the initial aggregates can possibly attach to the surface of a Au NP through pyridine/alkyl amine nitrogen bonding to the gold surface. It has been shown that organic amines such as 4-(dimethylamino) pyridine (DMAP) and oleyl amine act as favorite capping agents for aqueous Au NPs.[30,31] In this manner, an organic amine-rich thin layer can cover a Au NP surface, forming a new liquid-liquid interface next to the bulk aqueous homogeneous solution, the temperature of which is below the LCST.

Potential involvement of thermophoresis (thermodiffusion or Soret effect) which is a movement of molecules following the temperature gradient, was examined here as a mechanism of accumulation. It has been shown that the Soret effect leads to a distinct phase separation during the spinodal decomposition of a locally heated UCST (upper critical solution temperature) polymer blend[32] and that laser heating of a near-critical mixture leads to long-lasting patterns.[33,34] Also, the formation of a transient concentration cage around laser-heated Au NPs due to the Soret effect has been studied[35] and the formation of a transient network of a thermoresponsive polymer around a heated Au NP has been reported.[36] Given the temperature gradient, thermophobic molecules with a

16

positive Soret coefficient ($S_T > 0$) move to the cold area whereas thermophilic molecules with a

negative Soret coefficient ($S_T < 0$) move to the hot area.[37-39] The Soret coefficient, S_T, usually has a

positive sign in water.[40] Accordingly, molecules and particles are repelled from the hot regions.

However, the situation drastically changes when a liquid flow is applied simultaneously with the

temperature gradient.[41] In this situation, there is competition between the thermophoresis and the

phoretic motion in the direction of the external flow. The direction of particle migration can be

classified into three scenarios, schematically shown in **Scheme 3**.

Scheme 3. Schematic representation: the direction of particle migration under both external flow and
temperature gradient.
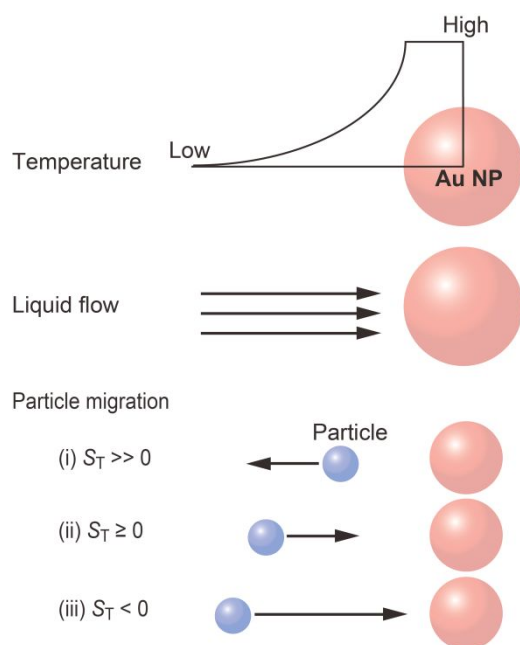
(i) Molecules are strongly thermophobic (S_T>>0), so they migrate against the liquid flow; (ii)

molecules are thermophobic ($S_T \geq 0$) but migrate along the liquid flow because of a weak

thermophoretic driving force; or (iii) molecules are thermophilic ($S_T < 0$) and migrate at an enhanced

velocity aided by the two driving forces. Experimentally, we found that lutidine and NiPPA molecules

migrated to a hot Au NP. At present, we are unaware of any reported Soret coefficients for these

molecules used in our experiments, so there are no clear data about the thermophilic/thermophobic

nature of these molecules. Nevertheless, even thermophobic molecules have been found to

17

accumulate around a hot Au NP. For instance, poly(N-isopropylacrylamide) (PNIPAM) molecules (well-recognized as a thermophobic polymer in aqueous solution[42,43]) accumulated and encapsulated a supported Au NP that was laser-heated.[44,45] The encapsulation occurred only while the Au NP was hot and the PNIPAM shell dissolved when laser illumination was terminated. Moreover, permanent accumulation encapsulating a Au NP was observed for sodium dodecyl sulfate (SDS) and polyethylene glycol (MW 6000) (PEG 6000),[46] on heating the Au NP for a few minutes through CW laser illumination. Both molecules have been reported to be thermophobic in aqueous solution.[47,48] These results suggest that thermodiffusion is not a prerequisite for the present observation of encapsulation of a hot Au NP. As we will describe below, transport of solutes through convective flow may surpass thermodiffusion. Such a possibility was demonstrated in section B by the observation of thermophobic PS particles being attracted toward a hot Au NP.

To interpret the droplet size dependency on laser intensity, one may simply assume that phase separation occurred in the region with temperatures above the LCST of the binary mixtures. The $1/r$ temperature profiles at various laser intensities near the threshold of droplet formation were calculated for 20-%w/w (4.0 mol%) lutidine/water and are shown in Supporting Information, Figure S10a. To demonstrate more clearly that diameter size above the LCST is dependent on laser intensity, Figure S10b plots the diameter occurring above the LCST vs. laser intensity, showing that the diameter sizes above the LCST are more than one order of magnitude greater than the droplet diameters observed (Figure 1e). Thus, the phase-separated microdroplet should be much denser than the solution and for the droplet to grow with illumination time and laser intensity, the transport of solutes (lutidine or NiPPA) must occur from outside the hot region adjacent to a Au NP, simultaneously with the expulsion of water molecules from the high-temperature area.

Our observation of the phoretic migration of PS particles strongly suggests the occurrence of liquid flow induced by Au NP heating. To investigate this assumption, we simulated liquid

18

flow inside the chamber (using COMSOL MultiPhysics) when supported Au NP is heated, (**Figure 4**). First, we assess a possible contribution of thermal convection, which can occur because particle-heating in a microfluidic chamber generates thermal convective flow from bottom to top and circulation inside the chamber because of buoyancy.[49] Figure 4a shows a simulated flow map of thermal convection in our microfluidic chamber for both ceiling (left) and floor (right) configurations. We found that the velocity of thermal convection for thin water films was much slower than that of thermocapillary flow (cf. Figure 4b and 4c). Moreover, we observed microdroplet formation encapsulating a Au NP regardless of the configuration of Au NP placed at two opposite sides of the chamber, ceiling and floor. The observation is contradictory to the major role of thermal convection in transporting lutidine or NiPPA in the direction of a Au NP because the former configuration is unfavorable for accumulating solutes in the vicinity of the Au NP.

When a phase separation of aqueous amines occurs adjacent to the Au NP, a liquid-liquid interface forms between the organic-rich droplet and the bulk solution. As a result, thermocapillary or thermal Marangoni convection can occur driven by the interfacial tension gradient.[50,51] The latter arises from the temperature gradient along the liquid-liquid interface between the lutidine-rich phase and the bulk solution[13] because the temperature of the droplet near the ceiling is higher than that of the droplet away from the substrate. This notion is supported by COMSOL simulation of 2D temperature distribution (Supporting Information S11, see below for further support). The interfacial tension increases with an increase in temperature[13] (as shown graphically in Supporting Information Figure S2-1d).
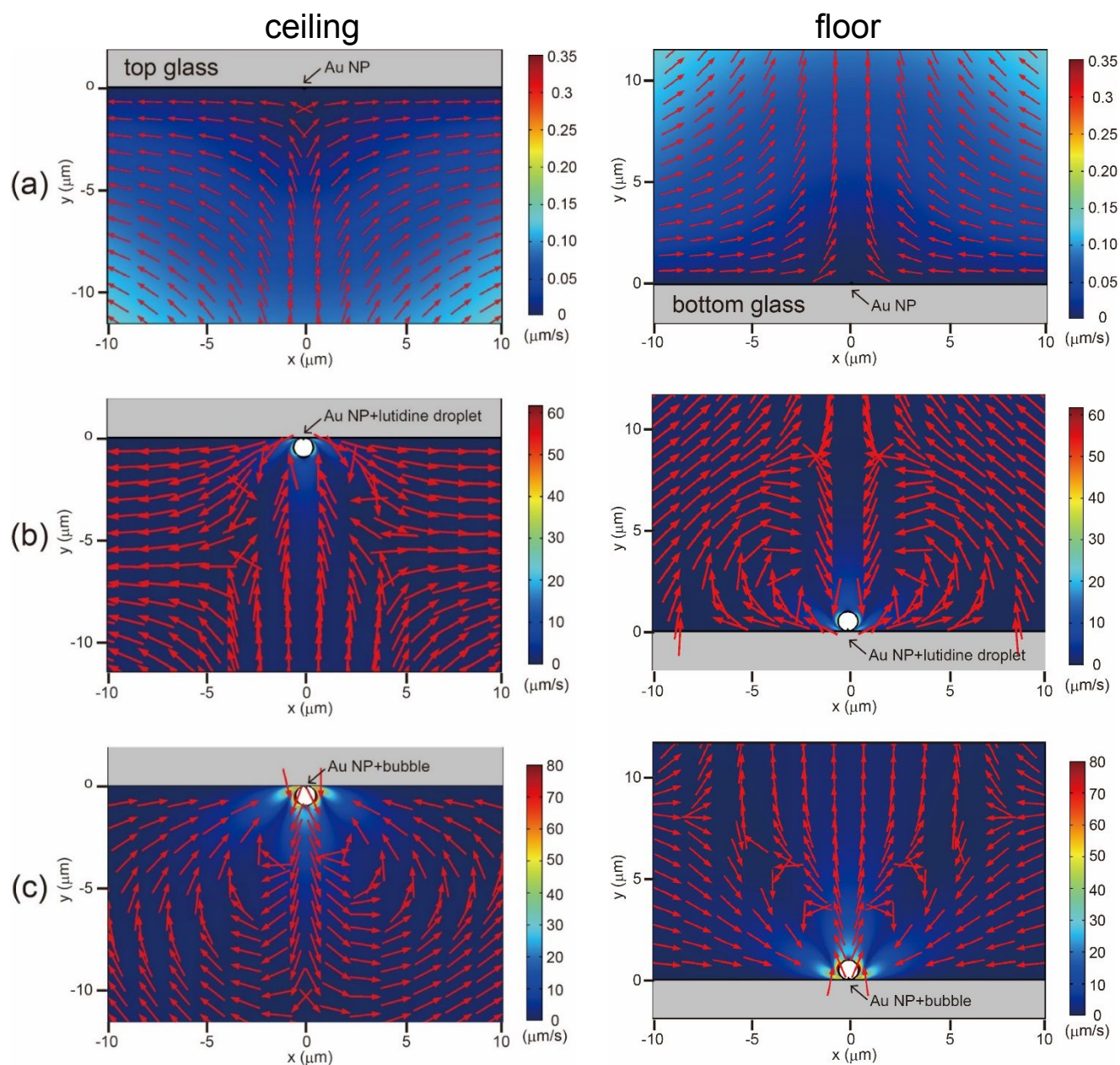
19

Figure 4. Simulated 2D convective velocity maps for a single water-immersed Au NP (100 nm in diameter) supported on a glass substrate for the ceiling (left) and floor (right) configurations (water film thickness: 200 μm). (a) Velocity distributions of thermal convection (input laser intensity: 1 mW μm^{-2}). (b) Velocity maps of thermal convection and Marangoni flow at the liquid/liquid interface of a lutidine-rich droplet (1-μm across) and bulk water. (input laser intensity: 1 mW μm^{-2}). (c) Velocity maps assuming both thermal convection in a closed chamber and Marangoni convection at the liquid water/vapor bubble (1-μm across) interface (input laser intensity: 10 mW μm^{-2}).

20

The temperature gradient from the hot substrate surface (where the Au NP is immobilized) to the cool apex of a lutidine-rich droplet generates a liquid flow around the lutidine-rich droplet when the Au NP is optothermally heated (Figure 4b). The simulation for the ceiling configuration predicts that a flow was generated inside the solution from the area below the Au NP to the droplet, deviating at the boundary between the droplet and the top substrate, then circulating, finally redirecting toward the droplet. This flow can convey solutes to the hot area, inducing their condensation, resulting in the growth of a phase-separated droplet. The calculated velocity of this thermocapillary flow was much greater than that of thermal convection (compare Figures 4a and 4b). For the floor configuration of a Au NP, the direction of flow is reversed.

Here we show evidence that the cause of asymmetric temperature distribution around a Au NP is the substrate: a droplet only forms in the solution encapsulating a hot Au NP and cannot penetrate into the substrate. The portion of a droplet directly attached to the substrate surface should be hotter than the apex away from the substrate, according to the simulation (Figure S11). In support of this assumption, we acquired a scanning electron microscope (SEM) image of a PNIPAM droplet encapsulating a supported Au NP (Supporting Information Figure S12). We depicted the PNIPAM droplet because it was difficult to capture the SEM image of a transient lutidine-rich or NiPPA-rich liquid droplet. Clearly, the PNIPAM shell grew asymmetrically around the supported Au NP. From this image, we can safely state that the PNIPAM droplet encapsulating a Au NP supported on a substrate can generate asymmetric temperature distribution leading to phase separation on heating the Au NP.

The droplet formation and growth are reminiscent of photothermal-bubble-induced trapping, in which colloids and molecules are attracted to the liquid-gas interface of a bubble driven by thermal Marangoni convection, as simulated in Figure 4c. Previously, photothermal bubbles have been generated by heating a metallic thin film deposited on a substrate.[52-56] As a result of optothermal trapping, fixation of fluorescent molecules, quantum dots and colloidal particles on the substrate are observed.[53] Furthermore, liquid-liquid phase-separation-induced crystallization of glycine has been

21

demonstrated.[53] For bubble-induced trapping, however, the direction of Marangoni flow given in Figure 4c is different from the direction of the flow in the phase separation-induced droplet growth shown in Figure 4b. For the ceiling configuration, the direction of flow is along the top wall to the droplet, deviating downwards, then circulating; finally being redirected toward the bubble. The simulated flow picture is consistent with the experimental phoretic flow of aqueous silica particles in a previous study.[27] At the interface between air and water of a photothermal bubble, the surface tension decreases with increasing temperature.[52-56] The thermal Marangoni convection principle predicts the flow from the hot Au NP side of the bubble to the cool apex of the photothermal bubble, which is consistent with the simulated and observed direction of flow. The simulation suggests that the maximum flow velocity calculated at 10 mW μm^{-2} (Figure 4c) is similar to that in Figure 4b at 1.0 mW μm^{-2}. The maximum flow velocities in Figures 4b and 4c are two orders of magnitude greater than that calculated for thermal convection in Figure 4a. The maximum velocities calculated were not affected by the Au NP configuration.

Without heating a Au NP, no microdroplets are observed. For instance, a focused illumination on the surface of a glass substrate at 10 mW μm^{-2}, which is at least 50-times greater in intensity than the threshold intensity of lutidine/water phase separation, did not result in the observation of microdroplets. This may mean that the contribution of optical forces is not so great although optical trapping cannot be completely eliminated at much higher laser intensities. Previously, the laser-induced phase separation of a binary mixture, aqueous triethylamine (TEA), has been demonstrated on irradiating with a focused 1064-nm laser light (~1 μm spot diameter and ~1.5 W power).[57,58] A TEA-rich droplet with a diameter of ~10 μm was formed at the laser focus and the driving force of the droplet formation and growth was ascribed to the optical gradient force that collects dissolved TEA molecules to the laser focus owing to a refractive index higher than that of water. Moreover, one study has pointed out the necessity of demixing transition at temperatures above the LCST to form a TEA-rich droplet.[57] In that study, heat generation occurred through absorption of a 1064-nm laser light by H_2O at the focal spot. In contrast, the transport of more distant molecules has nearly

been ignored even for formation of droplets with diameters far surpassing the beam diameter. Concerning the optical trapping of macromolecules and colloids it was not until recently that the positive role of molecular transport from the outer regions of the laser focus through convective flows has become a topic of discussion.[59] In other studies, the phase separation of lutidine/water adjacent to a Janus particle (gold half-coated silica sphere) under laser illumination was used to stimulate self-propelled motion of the particle.[60,61] The details of such local heating-induced phase separation has remained unexplored, however.

Finally, we summarize the current status of microscale optothermal flow generation applicable to separation and sorting of molecules, NPs and colloids. The important mechanism is a thermocapillary flow generated by the surface tension gradient. Such a flow is highlighted, in particular, at small scales because of the scale effect, although thermal convection can generate only a weak drag force in microfluidic systems.[62-64] **Scheme 4** shows the working principle for generating thermocapillary flow to drive particle transport in microfluidic systems. For example, when an IR or a near IR laser is focused into a water or glass-water interface (panel A), the laser light absorbed either by water or by solutes generated thermocapillary convective flow driven by the surface-tension gradient at the liquid water-air interface (*i.e.* the free surface). The flow drags colloids and molecules toward the laser focus. In an extreme case, when the illumination was focused at the liquid-air interface, the thermal Marangoni effect caused surface depression in the illuminated area.[65,66] In panel B, a microbubble was formed at the hot spot generated by laser heating of light-absorbing films or solutes.[52-56] As a result, particles were drawn toward the bubble induced by Marangoni flow.

Panels C and D depict working models demonstrated in the present study. When laser illumination induces small-scale liquid-liquid phase separation because of temperature increase above the critical temperature in the medium surrounding a Au NP (panel C), thermal Marangoni convection currents are generated because of a temperature-dependent change in liquid-liquid interfacial tension. As a result, transport and accumulation occur at the hot area. More intriguingly, directional control

23

over the Marangoni convection can be performed by reversing the position of the Au NP in the chamber as shown in panel D.

Scheme 4. Working models of thermocapillary flow in microfluidic systems. (A) Water or glass-water interface heating-induced generation of thermocapillary convective flow driven by the surface tension gradient at the liquid-water interface (free surface). (B) Marangoni convection around a microbubble formed at the hot spot generated by laser heating of light-absorbing films or solutes. (C) Thermal Marangoni convection currents induced by liquid-liquid interface surrounding the Au NP. (D) Reversed direction of thermocapillary convection, when the position of the Au NP in the chamber is reversed from that in C.

(A)

(B)

(C)

(D)

24
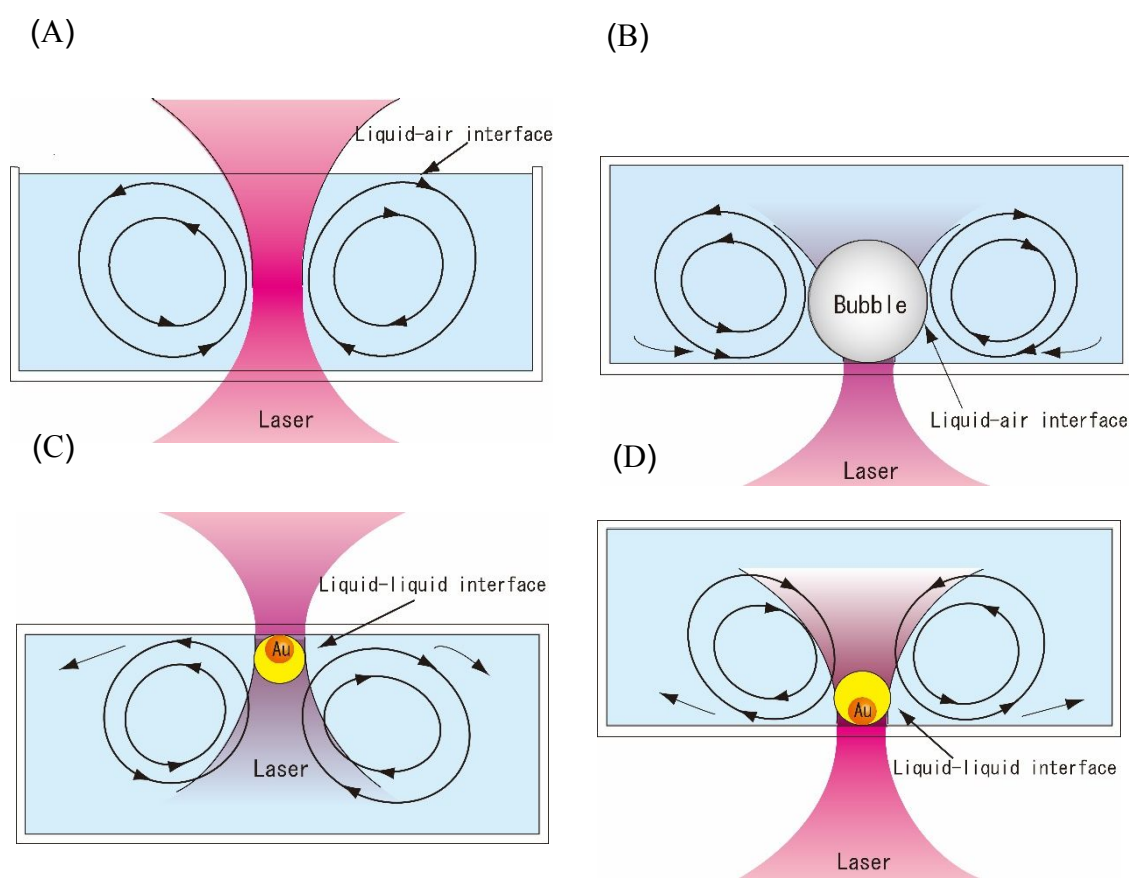
Conclusions

In this study, we have demonstrated single Au NP heating-induced phase separation of binary mixtures (exemplified by aqueous lutidine and *N*-isopropylpropionamide), resulting in transient formation of an organic-rich nano- to micro-meter sized droplet encapsulating the heated Au NP. The location-specific demixing behavior was characterized by using dark-field microscopy, light-scattering spectroscopy and Raman spectroscopy. At the beginning, thermal confinement within a concentric temperature gradient generated around a hot Au NP enables the spatial confinement of the demixing transition, resulting in the aggregation of solutes at temperatures above the LCST and the expulsion of water molecules. Then, a liquid-liquid interface surrounding the Au NP forms between the organic phase and bulk solution. At the liquid-liquid interface, asymmetric temperature distribution occurs and generates a thermocapillary flow driven by the surface-tension gradient. The existence of such a flow was demonstrated by observing the phoretic migration of polystyrene microparticles. We deduced that thermocapillary flow is responsible for the transport of more distal solute molecules to the high-temperature area adjacent to the Au NP surface, resulting in phase-separated droplet formation. The photothermal microfluidic flow generation demonstrated here is applicable to separation and sorting of colloids and macromolecules from solution with much less energy than with the use of optical tweezers.

■ ASSOCIATED CONTENT

Supporting Information

The Supporting Information is available free of charge on the ACS Publications website at DOI:

10.1021/acs.jpcc.

TEM image and histogram of Au NPs; physical properties including the phase diagrams of lutidine/water and NiPPA/water; details of the experimental and simulation methods; COMSOL details; lutidine concentration *vs.* scattering peak wavelength; scattering spectral simulation using Mie calculation; Raman spectroscopy under Au NP heating; sequence photos of particle tracking; calculated particle temperature as a function of laser intensity; size of areas above LCST; simulated 2D temperature distribution around a Au NP, SEM image of a PNIPAM droplet (PDF)

A movie showing the migration of PS particles (AVI).

■ AUTHOR INFORMATION

Corresponding Author

E-mail: hashichem@tokushima-u.ac.jp; hashichem@gunma-ct.ac.jp

ORCID

Takayuki Uwada: 0000-0003-4272-7964

Shuichi Hashimoto: 0000-0002-8020-5537

Author Contributions

I.A. and T.K. performed optical measurements. C.M. performed material synthesis and physical characterization. T.U. performed a numerical simulation. S.H. designed the experiment and prepared the manuscript with contributions from all authors. All authors have given approval to the final version of the manuscript.

Notes

The authors declare no competing financial interest.

■ ACKNOWLEDGMENTS

References

1. Keating, C. D. Aqueous Phase Separation as a Possible Route to Compartmentalization of Biological Molecules. *Acc. Chem. Res*. **2012**, *45*, 2114–2124.

2. Hyman, A. A.; Weber, C. A.; Jülicher, F. Liquid-Liquid Phase Separation in Biology. *Annu. Rev. Cell Dev. Biol*. **2014**. *30*, 39–58.

3. Falahati, H,; Haji-Akbar, A. Thermodynamically Driven Assemblies and Liquid–Liquid Phase Separations in Biology. *Soft Matter*, **2019**, *15*, 1135–1154.

4. ten Wolde, R. E.; Frankel, D. Enhancement of Protein Crystal Nucleation by Critical Density Fluctuations. *Science* **1997**, *277*, 1975-1978.

5. Vekilov, P. G. Dense Liquid Precursor for the Nucleation of Ordered Solid Phases from Solution. *Cryst. Growth Des*. **2004**, *4*, 671-685.

6. Dolgin, E. Cell Biology's New Phase. Nature **2018**, *555*,300–302.

7. Shin, Y.; Brangwynne, C. P. Liquid Phase Condensation in Cell Physiology and Disease. *Science*. **2017**, *357*, eaaf4382.

8. Banani, S. F.; Lee, H. O.; Hyman, A. A.; Rosen, M. K. Biomolecular Condensates: Organizers of Cellular Biochemistry. *Nat. Rev. Mol. Cell. Biol*. **2017**, *18*, 285–298.

9. Toyouchi, S.; Kajimoto, S.; Toda, M.; Fukumura, H.; Kawakatsu, T.; Akama, Y.; Kotani, M. Time-Resolved Structured Illumination Microscopy for Phase Separation Dynamics of Water and 2‑Butoxyethanol Mixtures: Interpretation of "Early Stage" Involving Micelle-Like Structures. *J. Phys. Chem. B* **2018**, *122*, 12375−12385.

10. Roy, S.; Dietrich, S.; Maciołek, A. Solvent Coarsening around Colloids Driven by Temperature

27

Gradients. *Phys. Rev. E*, **2018**, *97*, 042603.

11. Keblinski, P.; Cahill, D. G.; Bodapati, A.; Sullivan, C. R.; Taton, T. A. Limits of Localized Heating by Electromagnetically Excited Nanoparticles. *J. Appl. Phys.* **2006**, *100*, 054305.

12. Loven, A. W.; Rice, O. K. Coexistence Curve of the 2,6-Lutidine+Water System in the Critical Region. *Faraday Soc. Trans*. **1963**, *59*, 2723−2727.

13. Grattoni, C. A.; Dawe, R. A.; Seah, C. Y.; Gray, J. D. Lower Critical Solution Coexistence Curve and Physical Properties (Density, Viscosity, Surface Tension, and Interfacial Tension) of 2,6-Lutidine + Water, *J. Chem. Eng. Data* **1993**, *38*, 516–519.

14. Mirzaev, S. Z.; Behrends, R.; Heimburg, T.; Haller, J.; Kaatze, U. Critical Behavior of 2,6-Dimethylpyridine-Water: Measurements of Specific Heat, Dynamic Light Scattering, and Shear Viscosity. *J. Chem. Phys*. **2006**, *124*, 144517.

15. Geukens, B.; Meersman, F.; Nies, E. Phase Behavior of *N*-(Isopropyl)propionamide in Aqueous Solution and Changes in Hydration Observed by FTIR Spectroscopy. *J. Phys. Chem. B* **2008,** *112,* 4474-4477.

16. Hashimoto, C.; Nagamoto, A.; Maruyama, T.; Kariyama,N.; Irisa, Y.; Ikehata ,A.; Ozaki, Y. Hydration States of Poly(N‑isopropylacrylamide) and Poly(N,N‑diethylacrylamide) and Their Monomer Units in Aqueous Solutions with Lower Critical Solution Temperatures Studied by Infrared Spectroscopy. *Macromolecules* **2013**, *46*, 1041−1053.

17. Marczak, W.; Kiełek, K.; Czech,B.; Flakusa, H.; Rogalski, M. Complexes of 2,6-Dimethylpyridine with Water in Condensed Phases and the Dynamical Co-operative Interactions Involving Hydrogen Bonds. *Phys. Chem. Chem. Phys*. **2009**, *11*, 2668–2678.

18. Baffou, G. *Thermoplasmonics Heating Metal Nanoparticles Using Light*; Cambridge University Press: Cambridge, UK, 2017.

19. Qin, Z.; Bischof, J. C. Thermophysical and Biological Responses of Gold Nanoparticle Laser Heating. *Chem. Soc. Rev.* **2012**, *41*, 1191–1217.

20. Norton, S. J.; Vo-Dinh, T. Photothermal Effects of Plasmonic Metal Particles in a Fluid. *J. Chem.*

28

Phys. **2016**, *119*, 083105.

21. Gharatape, A.; Davaran, S.; Salehi, R.; Hamishehkar, H. Engineered Gold Nanoparticles for Photothermal Cancer Therapy and Bacteria Killing. *RSC Adv*. **2016**, *6*, 111482–111516.

22. Mayer, K. M.; Hafner, J. H. Localized Surface Plasmon Sensors. *Chem. Rev*. **2011**, *111*, 3828–3857.

23. Bohren, C. F.; Huffman, D. R. *Absorption and Scattering of Light by Small Particles*; Wiley: New York, 1983.

24. Setoura, K.; Werner, D; Hashimoto, S Optical Scattering Spectral Thermometry and Refractometry of a Single Gold Nanoparticle under CW Laser Excitation. *J. Phys. Chem. C*, **2012**, *116*, 15458–15466.

25. Helden, L; Eichhorn, R.; Bechinger, C. Direct Measurement of Thermophoretic Forces. *Soft Matter*, **2015**, *11*, 2379–2386.

26. Tsuji, T.; Kozai, K.; Ishino, H.; Kawano, S. Direct Observations of Thermophoresis in Microfluidic Systems. *Micro Nano Lett*., **2017**, *12*, 520–525.

27. Chikazawa, J.; Uwada, T.; Furube, A.; Hashimoto, S. Flow-Induced Transport via Optical Heating of a Single Gold Nanoparticle. *J. Phys. Chem. C* **2019**, *123*, 4512−4522.

28. Carattino, A.; Caldarola, M. Orrit, M. Gold Nanoparticles as Absolute Nanothermometers. *Nano Lett*. **2018**, *18*, 874−880.

29. Jones, S.; Andrên, D.; Karpinski, P.; Käll, M. Photothermal Heating of Plasmonic Nanoantennas: Influence on Trapped Particle Dynamics and Colloid Distribution. *ACS Photonics* **2018**, *5*, 2878−2887.

30. Aslam, M.; Fu, L.; Su, M.; Vijayamohanan, K.; Dravid, V. P. Novel One-step Synthesis of Amine-stabilized Aqueous Colloidal Gold Nanoparticles. *J. Mater. Chem*., **2004**, *14*, 1795–1797.

31. Gandubert, V. J.; Lennox, R. B. Assessment of 4-(Dimethylamino)pyridine as a Capping Agent for Gold Nanoparticles. *Langmuir*, **2005**, *21*, 6532–6539.

32. Voit, A.; Krekhov, A.; Enge, W.; Kramer, L.; Köhler, W. Thermal Patterning of a Critical

29

Polymer Blend. *Phys. Rev. Lett.* 2005, 94, 214501.

33. Voit, A.; Krekhov, A.; Köhler, W. Laser-induced structures in a polymer blend in the vicinity of the phase boundary. *Phys. Rev. E*, 2007, 76, 011808.

34. Köhler, W.; Krekhov, A.; Zimmermann, W. Thermal Diffusion in Polymer Blends: Criticality and Pattern Formation. *Adv. Polym. Sci*. 2010, 227, 145−198.

35. Schwaiger, F.; Zimmermann, W.; Köhler, W. Transient Cage Formation Around Hot Gold Colloids Dispersed in Polymer Solutions. *J. Chem. Phys*. 2011, 135, 224905.

36. Orlishausen, M.; Köhler, W. Forced Phase Separation by Laser-Heated Gold Nanoparticles in Thermoresponsive Aqueous PNIPAM Polymer Solutions. *J. Phys. Chem. B* 2015, 119, 8217−8222.

37. Duhr, S.; Braun, D. Why Molecules Move along a Temperature Gradient. *Proc. Natl Acad. Sci. USA*, **2006**, *103*. 19678−19682.

38. Piazza, R. Thermophoresis: Moving Particles with Thermal Gradients. *Soft Matter*, **2008**, *4*, 1740−1744.

39. Würger A. Thermal Non-equilibrium Transport in Colloids. *Rep. Prog. Phys,* **2010**, 73, 126601.

40. Fränzl, M.; Thalheim, T.; Adler, J.; Huster, D.; Posseckardt, J.; Mertig, M.; Cichos, F. Thermophoretic trap for single amyloid fibril and protein aggregation studies. *Nature Methods* **2019**, 16, 611−614.

41. Tsuji, T.; Sasai, Y.; Kawano, S. Thermophoretic Manipulation of Micro- and Nanoparticle Flow through a Sudden Contraction in a Microchannel with Near-Infrared Laser Irradiation. *Phys. Rev. Appl.* **2018**, *10*, 044005.

42. Kita, R.; Wiegand, S. Soret Coefficient of Poly(N-isopropylacrylamide)/Water in the Vicinity of Coil-Globule Transition Temperature. *Macromolecules* 2005, 38, 4554−4556.

43. Wongsuwarn, S.; Vigolo, D.; Cerbino, R.; Howe, A. M.; Vailati, A.; Piazza, R.; Cicuta, P. Giant Thermophoresis of Poly(Nisopropylacrylamide) Microgel Particles. *Soft Matter* 2012, 8, 5857−5863.

30

44. Aibara, I.; Mukai, S.; Hashimoto, S. Plasmonic-Heating-Induced Nanoscale Phase Separation of Free Poly(*N*-isopropylacrylamide) Molecules. *J. Phys. Chem. C*, **2016**, *120*, 17745–17752.

45. Aibara, I.; Chikazawa, J..; Uwada, T.; Hashimoto, S. Localized Phase Separation of Thermoresponsive Polymers Induced by Plasmonic Heating. *J. Phys. Chem. C*, **2017**, *121*, 22496–22507.

46. Enders, M.; Mukai, S.; Uwada, T.; Hashimoto, S. Plasmonic Nanofabrication through Optical Heating. *J. Phys. Chem. C*, **2016**, *120*, 6723–6732.

47. Chan, J.; Popov, J. J.; Kolisnek-Kehl, S.; Leaist, D. G. Soret Coefficients for Aqueous Polyethylene Glycol Solutions and Some Tests of the Segmental Model of Polymer Thermal Diffusion. *J. Solution Chem*. 2003, 32, 197−214.

48. Vigolo, D.; Buzzaccaro, S.; Piazza, R. Thermophoresis and Thermoelectricity in Surfactant Solutions. *Langmuir* 2010, 26, 7792−7801.

49. Flores-Flores, E.; Torres-Hurtado, S. A.; Páez, R.; Ruiz, U.; Beltrán-Pérez, G.; Neale, S. L.; Ramirez-San-Juan, J. C.; Ramos-García, R. Trapping and Manipulation of Microparticles using Laser-induced Convection Currents and Photophoresis. *Biomed. Opt. Express*, **2015**, *6*, 4079–4087.

50. Manjare, M.; Yang, F.; Qiao, R.; Zhao, Y. Marangoni Flow Induced Collective Motion of Catalytic Micromotors. *J. Phys. Chem. C* **2015**, *119*, 28361−28367.

51. Yang, X.; Baczyzmalski, D.; Cierpka, C.; Mutschke, G.; Eckert, K. Marangoni Convection at Electrogenerated Hydrogen Bubbles. *Phys. Chem. Chem. Phys.,* **2018**, *20*, 11542−11548.

52. Zheng, Y.; Liu, H.; Wang, Y.; Zhu, C.; Wang, S.; Cao, J.; Zhu, S. Accumulating Microparticles and Direct-writing Micropatterns using a Continuous-wave Laser-induced Vapor Bubble. *Lab Chip* **2011**, *11*, 3816–3820.

53. Uwada, T.; Fujii, S.; Sugiyama, T.; Usman, A.; Miura, A.; Masuhara, H.; Kanaizuka, K.; Haga, M. Glycine Crystallization in Solution by CW Laser-Induced Microbubble on Gold Thin Film Surface. *ACS Appl. Mater. Interfaces* **2012**, *4*, 1158−1163.

31

54. Roy, B.; Arya, M.; Thomas, P.; Jürgschat, J. K.; Rao, K. V.; Banerjee, A.; Reddy, C.M.; Roy, S. Self-Assembly of Mesoscopic Materials to Form Controlled and Continuous Patterns by Thermo-Optically Manipulated Laser Induced Microbubbles. *Langmuir* **2013**, *29*, 14733–14742.

55. Hu, W.; Fan, Q.; Ohta, A. T. An Opto-thermocapillary Cell Micromanipulator. *Lab Chip* **2013**, *13*, 2285–2291.

56. Lin, L.; Peng, X.; Mao, Z.; Li, W.; Yogeesh, M. N.; Rajeeva, B. B.; Perillo, E. P.; Dunn, A. K.; Akinwande, D.; Zheng, Y. Bubble-Pen Lithography. *Nano Lett*. **2016**, *16*, 701−708.

57. Kitamura, N.; Yamada, M.; Ishizaka, S.; Konno, K. Laser-Induced Liquid-to-Droplet Extraction of Chlorophenol: Photothermal Phase Separation of Aqueous Triethylamine Solutions. *Anal. Chem*. **2005**, *77*, 6055–6061.

58. Mukai, S.; Magome, N.; Kitahara, H.; Yoshikawa, K. Liquid-Liquid Dynamic Phase Separation Induced by a Focused Laser. *Appl. Phys. Lett*. **2003**, *83*, 2557–2559.

59. Louchev, O. A.; Juodkazis, S.; Murazawa, N.; Wada, S.; Misawa, H. Coupled Laser Molecular Trapping, Cluster Assembly, and Deposition Fed by Laser-induced Marangoni Convection. *Opt. Express* **2008**, *16*, 5673–5680.

60. Volpe, G.; Buttinoni, I.; Vogt, D.; Kümmerer, H.-J.; Bechinger, C. Microswimmers in Patterned Environments. *Soft Matter*, 2011, 7, 8810−8815.

61. Buttinoni, I.; Volpe, G.; Kümmel, F.; Giorgio Volpe, G.; Bechinger, C. Active Brownian Motion Tunable by Light. *J. Phys.: Condens. Matter* 2012, 24, 284129.

62. Vera, E.; Hafez, M.; Régnier, S. Laser-Induced Thermocapillary Convection for Mesoscale Manipulation. *Int. J. Optomechatron.* **2009**, *5*, 289−302.

63. Baigl, D. Photo-actuation of Liquids for Light-driven Microfluidics: State of the Art and Perspectives. *Lab Chip* **2012**, *12*, 3637–3653.

64. Quispe, J.; Elvin Muńoz, E.; Vela, E. Exploiting the Transient Behavior of Thermocapillary Convection Flows to Enhance Non-contact Mesoscale Manipulation. *Appl. Phys. Lett*. **2016**, *109*, 124102.

65. Ortega-Mendoza, J. G.; Sarabia-Alonso, J. A.; Zaca-Morán, P.; Padilla-Vivanco, A.; Toxqui-Quitl, C.; Rivas-Cambero, I.; Ramirez-Ramirez, J.; Torres-Hurtado, S. A.; Ramos-García, R. Marangoni Force-driven Manipulation of Photothermally-induced Microbubbles. *Opt. Express* **2018**, 26, 6653−6662.

66. Gugliotti, M.; Baptista, M. S.; Politi, M. J. Laser-Induced Marangoni Convection in the Presence of Surfactant Monolayers. *Langmuir* **2002**, *18*, 9792–9798.

Graphical abstract